Tunable valleytronics with symmetry-retaining high polarization degree in SnS_xSe_{1-x} model system

Shuren Lin, Zixuan Fang, Tingzheng Hou (iD), Ting Wan Hsu, Chi H. So, Cher Yeoh, Roger Li, Yin Liu, Emory M. Chan, Yu-Lun Chueh, Bin Tang, Kristin Persson, and Jie Yao (iD)

View Online   Export Citation   CrossMark

ARTICLES YOU MAY BE INTERESTED IN

Enhanced surface superconductivity in $Ba(Fe_{0.95}Co_{0.05})_2As_2$
Applied Physics Letters **116**, 062601 (2020); https://doi.org/10.1063/1.5133647

Integration of polycrystalline Ga_2O_3 on diamond for thermal management
Applied Physics Letters **116**, 062105 (2020); https://doi.org/10.1063/1.5125637

Impact of the thermal environment on the analog temporal response of HfO_x–based neuromorphic devices
Applied Physics Letters **116**, 063504 (2020); https://doi.org/10.1063/1.5139627

Tunable valleytronics with symmetry-retaining high polarization degree in SnS_xSe_{1-x} model system

View Online   Export Citation   CrossMark

Shuren Lin,[1,2] Zixuan Fang,[1,3] Tingzheng Hou,[1,4] (iD) Ting Wan Hsu,[1,5] Chi H. So,[1] Cher Yeoh,[1] Roger Li,[1] Yin Liu,[1,2] Emory M. Chan,[2] Yu-Lun Chueh,[5,6] Bin Tang,[3] Kristin Persson,[1,4] and Jie Yao[1,4,7,a]] (iD)

AFFILIATIONS

[1]Department of Materials Science and Engineering, University of California, Berkeley, California 94720, USA
[2]The Molecular Foundry, Lawrence Berkeley National Laboratory, Berkeley, California 94720, USA
[3]National Engineering Research Center of Electromagnetic Radiation Control Materials, State Key Laboratory of Electronic Thin Films and Integrated Devices, University of Electronic Science and Technology of China, Chengdu 611731, People's Republic of China
[4]Materials Sciences Division, Lawrence Berkeley National Laboratory, Berkeley, California 94720, USA
[5]Department of Materials Science and Engineering, National Tsing Hua University, Hsinchu 30013, Taiwan
[6]State Key Laboratory of Advanced Processing and Recycling of Non-Ferrous Metals, Lanzhou University of Technology, School of Materials Science and Engineering, Lanzhou University of Technology, Lanzhou 730050, People's Republic of China
[7]Tsinghua-Berkeley Shenzhen Institute, University of California, Berkeley, California 94720, United States

[a]]Author to whom correspondence should be addressed: yaojie@berkeley.edu

ABSTRACT

SnS has recently been shown to possess unique valleytronic capability with a large polarization degree, where non-degenerate valleys can be accessed using linearly polarized light, bestowed upon by the unique anisotropy and wavefunction symmetry. It is thus of utmost importance to demonstrate the extension of such effects for the IV–VI system in general, thereby elucidating the generality and tunability of such valleytronics. We show the highly tunable valleytronics via gradual compositional control of the tin(II) sulfo-selenide (SnS_xSe_{1-x}) alloy system with excellent retainment of symmetry-determined selection rules. We show the presence of both ΓY and ΓX valleys in all alloy compositions via selectivity in absorption and emission of linearly polarized light by optical reflection (R)/transmission (T) and photoluminescence measurements and tuned the bandgaps of the valleys within a range of 1.28 eV–1.05 eV and 1.48 eV–1.24 eV, respectively. This simultaneous tuning of non-degenerate valleys agrees well with theoretical calculations. We then fitted the bandgap values in compositional space, obtaining bowing parameters as a useful database. We further demonstrated the feasibility of using IV–VI valleytronics systems in general by elucidating the retainment of strong polarization degrees of as high as 91% across all compositions. The generalization of such purely symmetry-dependent valleytronics also opens up opportunities for the discovery of more multi-functional materials.

Published under license by AIP Publishing. https://doi.org/10.1063/1.5128717

The field of valleytronics presents great opportunities in providing an additional valley degree of freedom in the control of electronic systems;[1,2] much promise in utilizing this unique material's or system's properties hinges upon the ability to access and hence control each valley selectively. Earlier work on valleytronics demonstrated the selective population of degenerate conduction band minima, using strong biases, in systems such as Si,[3,4] AlAs,[5,6] and diamond.[7] More recently, theoretical work on graphene valleytronics[8] has led to the exploration of valleytronics in two-dimensional (2D) systems.

One of the most effective and well-exploited ways to explore the valleys of a material is to leverage the light–matter interaction; in essence, certain polarization of light is used to selectively populate each valley, which can then form different population states where on–off information can be subsequently utilized. Previous reports of valleytronic behavior on 2D transition metal dichalcogenides (TMDCs) have demonstrated selective optical valley excitation with varying degrees of success.[9–12] These reports have generated renewed interest in the valleytronic field, one of which being the actual

manipulation of valley population under ambient and bias-free conditions with a high polarization degree, which was only recently reported,[13] where we demonstrated a form of valleytronics in tin(II) sulfide (SnS).

Such valleytronics has a twofold manifestation. First, the two sets of valleys in SnS reside along the ΓY and ΓX directions in reciprocal space, respectively, and, by the selection rules, are exclusively selected by y and x polarized light, respectively (supplementary material, Text S1, adapted from Ref. 13). Second, the anisotropic nature of the material bestows upon the valleys the non-degeneracy in bandgap values. As such, both incident light polarization and energy can potentially be used to independently access each valley, granting the material system more flexibility in terms of excitation conditions.

An important extension to such flexibility is then to expand such valleytronics to the rest of the IV–VI family, which will not only allow a wider wavelength range for excitation/emission but, more importantly, prove that such valleytronics is a general behavior within the material system.

Herein, we report a model system in SnS_xSe_{1-x}, $0 \leq x \leq 1$, demonstrating both the retainment of valley selectivity and the gradual tuning of bandgaps at both valleys across all alloy compositions. The retainment of photoluminescence (PL) intensity and polarization degrees across the whole compositional range proves that members of the SnS_xSe_{1-x} family are suitable for such valleytronics in general.

We also demonstrate the continuous tuning of bandgaps for both valleys across the whole compositional range; the range of bandgaps (1.28 eV–1.05 eV and 1.48 eV–1.24 eV for the two valleys, respectively) is much larger than that of 2D semiconductor alloys,[14–17] especially when considering the combined effects of both valleys under different polarizations. Furthermore, typical advantages of semiconductor alloys over pure semiconductors, including the flexibility in choice of synthesis methods[16] and the additional parameter of lattice matching,[18] can be utilized on top of bandgap tunability.

SnS_xSe_{1-x} was chosen because of the similarity in band structures for SnS and SnSe, with the presence of two valleys along the ΓY and ΓX axes and the band separation at the Γ point having a larger value than the two valleys.[19] Since both materials' band structures arise from combinations of the same constituent wavefunctions,[20] which satisfies the same symmetry considerations,[21] valley selection rules in SnS have to also apply to SnSe, along with all SnS_xSe_{1-x} compositions.

Both SnS and SnSe have the Pmcn crystal structure with an orthorhombic unit cell comprising puckered layers,[22] and the lattice parameters of SnS_xSe_{1-x} have been experimentally shown to vary gradually across the alloy compositions.[23] The 2×2 supercells of SnS, SnSe, and a representative $SnS_{0.5}Se_{0.5}$ alloy are presented in Fig. 1(a). Using the fitted lattice parameters from Ref. 23 and adopting the simplest case of homogeneous alloying,[16] our density functional theory (DFT) calculations yield band structures with two local bandgaps along the ΓY and ΓX axes, denoted by $E_{g,\Gamma Y}$ and $E_{g,\Gamma X}$, respectively, across the whole compositional range (Figs. 2 and S1).

We synthesized SnS_xSe_{1-x} microplates, $0 \leq x \leq 1$ in nominal increments of $\Delta x = 0.125$ via physical vapor deposition (PVD), and observed their flat morphology via SEM. Figure 1(b) shows the optical microscopy image, SEM image, and SEM-energy-dispersive x-ray spectroscopy (EDX) mappings of Sn, S, and Se of a representative nominally $SnS_{0.875}Se_{0.125}$ alloy (the peak intensities for S and Se in the SEM-EDX spectra and images and mapping results of other alloys are

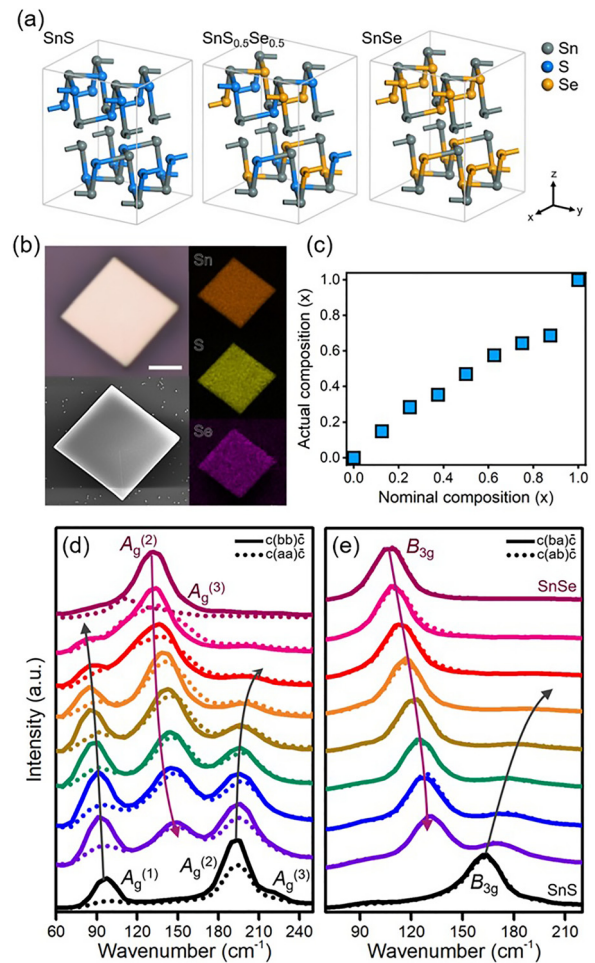**FIG. 1.** Structure and characterization of SnS_xSe_{1-x}. (a) 2×2 supercells of molecular structures of SnS, SnSe, and a representative $SnS_{0.5}Se_{0.5}$ alloy with the simplest case of homogeneous alloying. The puckered arrangement of atoms and the high anisotropy along the y (armchair) and x (zigzag) directions are maintained across the whole compositional range, while the lattice parameters increase with the Se content. (b) Optical microscopy image, scanning electron microscopy (SEM) images, and energy-dispersive x-ray spectroscopy (EDX) maps of a representative, nominally $SnS_{0.875}Se_{0.125}$ sample, demonstrating a flat surface and homogeneous distribution of Sn, S, and Se. The scale bar is 5 μm. (c) Trend in the actual composition vs nominal (design) composition, showing a general excess of the Se content. (d) Reflection mode, $c(xx)\bar{c}$, Raman spectra obtained under parallel polarization. The first and second letters in the parentheses denote the alignment of the incident light and emitted signal. Only spectra aligned along x and y directions are presented, showing clear trends in intensities for the A_g modes, thus ascertaining the identity and orientation of the measured samples. (e) Raman spectra obtained under cross polarization, showing clear trends in intensities for the B_{3g} modes.

presented in Figs. S2 and S3, respectively). The exact S:Se ratios obtained from SEM-EDX follow a gradual trend and were used for quantitative analysis.

From the plot of actual composition vs nominal (design) composition [Fig. 1(c)], we can see that the Se content of all compositions is consistently higher than the design amount. This can be attributed to the lower equilibrium vapor pressure of SnSe as compared with
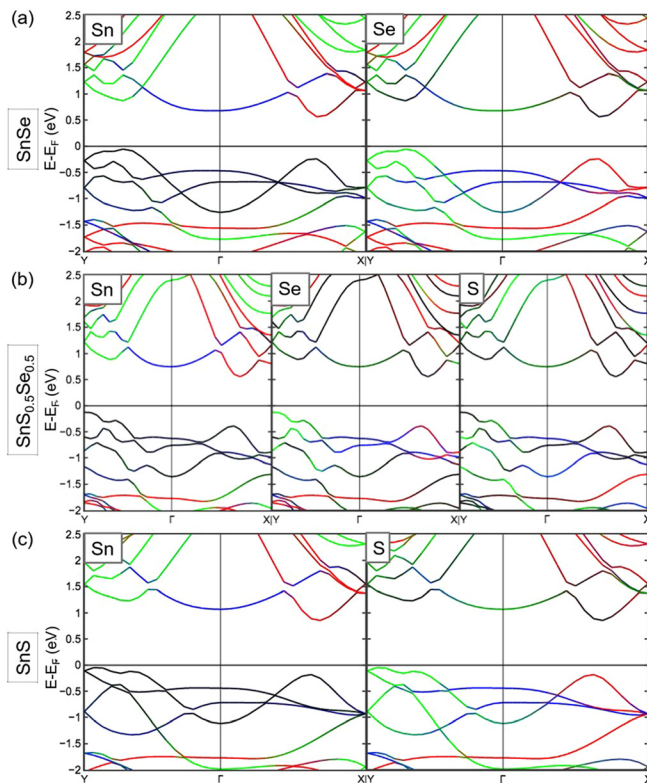
FIG. 2. Calculated band structures for selected SnS$_x$Se$_{1-x}$. Orbital projected band structures along Y-Γ-X and DOS of representative alloy compositions of (a) SnSe, (b) SnS$_{0.5}$Se$_{0.5}$, and (c) SnS are presented. Band structures are projected on the elements of Sn, S, and Se and p$_x$, p$_y$, and p$_z$ orbitals. Our elemental and orbital specific band structures denote that for all alloy compositions, p orbitals from Sn and the chalcogenides make up predominantly the conduction and valence bands, respectively. Red, green, and blue shades correspond to contributions of each subband by p$_x$, p$_y$, and p$_z$ orbitals, respectively; this demonstrates that ΓX and ΓY valleys are predominantly made up of p$_x$ and p$_y$ orbitals, respectively, for all alloy compositions.

SnS,[24,25] which is commonly reflected in the higher required PVD growth temperature of SnSe as compared with SnS.[26,27] Our SEM-EDX results reflect the compositional tunability using our growth method. Further tuning, especially for a large S content, is beyond the scope of this work, but it should also be achievable using S compensation[28] or multi-sourced CVD methods.[29,30]

Raman spectra of SnS[26] and SnSe[27] under −z excitation (perpendicular to the layers) contain characteristic peaks that correspond to three A$_g$ modes and one B$_{3g}$ mode. We observed that these modes follow gradual shifts for the alloys [Figs. 1(d) and 1(e)]. Note that the composition values are nominal, not actual. The larger change in the actual composition from SnS to SnS$_{0.875}$Se$_{0.125}$ leads to a rapid change of B$_{3g}$ modes. We used the relative peak intensities[27] to determine the armchair (y) and zigzag (x) directions of each alloy composition and presented the respective spectra under 532 nm excitation when the incident polarization is aligned along the x and y axes for parallel [Fig. 1(d)] and cross [Fig. 1(e)] polarization configurations. Note that the peak for the A$_{1g}^{(1)}$ mode of SnSe cannot be observed due to the wavenumber being lower than the Raman filter edge. Also, for clarity,

Raman spectra aligned along the y axis under parallel excitation is repeated using 785 nm excitation to clearly distinguish and reveal the trends for the A$_{1g}^{(3)}$ modes of the alloys (Fig. S4).

We observed a clear two-mode behavior for all Raman peaks, where the alloys can exhibit two peaks (SnS-like and SnSe-like) that belong to the same Raman mode. This alloy behavior can be explained using the modified random element isodisplacement (MREI) model,[17,31] where strong S–Se interactions give two eigenvalues, one SnS-like, and one SnSe-like, as the solutions to the quadratic equation of the model. This observation agrees with the common understanding that SnS and SnSe possess comparable interlayer and intralayer forces, as evidenced by the relatively small difference in interlayer and intralayer atomic distances.[19] Since all of the Raman modes of concern here are related to relative interlayer motions,[27] S–Se interactions should be significant, which explains the two-mode behavior.

The tunability of bandgap values at each valley is demonstrated using reflection (R) and transmission (T), as well as PL measurements, following the same protocol in our previous work on SnS.[13] White light R and T measurements were conducted with the incident excitation polarized along the y or x direction, hence demonstrating valley selectivity for absorption. Normalized Tauc plots are presented in Fig. 3(a), clearly showing the decrease in optical bandgap values as the Se content increases. Using Tauc plot analyses, we show that the bandgaps can be gradually tuned within a range of 1.28 eV–1.05 eV and 1.48 eV–1.24 eV for the ΓX and ΓY valleys, respectively.

PL measurements were conducted under parallel or cross polarization, with a second polarizer serving as an analyzer placed before the detector, to further demonstrate selectivity for emission. Figure 3(b) shows the PL spectra under parallel polarized 532 nm excitation that is aligned to the y and x axes for all alloy compositions, which elucidates the presence of a single PL peak in each spectrum that corresponds to the ΓY and ΓX valleys, respectively. [Due to the limit of the silicon visible range detector, the PL peaks from the ΓX valleys cannot be detected for alloys with Se content SnS$_{0.25}$Se$_{0.75}$ (nominal) and above. We subsequently conducted PL measurements using 785 nm excitation and an InGaAs infrared detector (Fig. S5) to obtain the PL peak positions of those alloys.] It can be observed that the PL peak positions red shift with more Se for a range of 1.29 eV–1.20 eV and 1.64 eV–1.45 eV, respectively. This agrees with the decrease in optical bandgap values obtained from R and T spectra.

The trends in bandgaps values for the valleys can be explained using the difference in contributions of elemental atomic orbitals to the subbands that make up the conduction band minimum (CBM) and valence band maximum (VBM). Orbital projected band structures in Fig. 2 show that the CBMs are predominantly made up of 5p orbitals from Sn, while the VBMs are mainly composed of p orbitals of chalcogenide atoms. The contribution by Se is from the 4p orbitals, which is higher in energy as compared with the 3p orbitals of S. Therefore, with a greater Se content, the hybridized orbitals that make up the VBM of alloys will have more Se character, hence leading to a smaller bandgap. This is clearly shown in Fig. 2(b), where the VBM of SnS$_{0.5}$Se$_{0.5}$ is contributed mostly by Se orbitals.

The trends in bandgap values agree with the calculated band structure (Figs. 2 and S1), ascertaining the validity of the optical measurement results. More importantly, our DFT calculations show that the CBM and VBM along ΓX (ΓY) are contributed almost entirely by

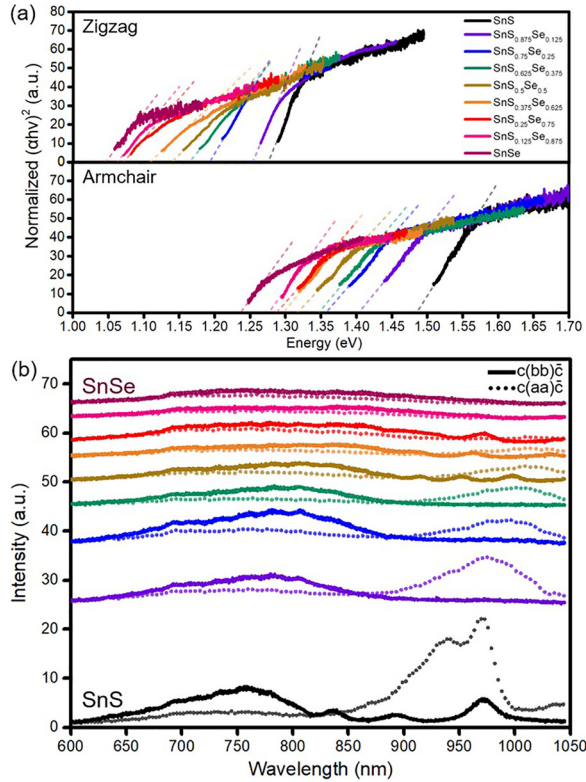**FIG. 3.** Optical measurements of SnS$_x$Se$_{1-x}$. (a) Normalized Tauc plots of both directions for different alloy compositions obtained from white light R and T measurements, showing a distinct decrease in the bandgap value with the increasing Se content. (b) PL peaks under parallel polarization. Only spectra aligned along x and y directions are presented, showing that for all alloy compositions, the high (low) energy peak has the strongest intensity when the excitation light is polarized along the y (x) direction, showing the retainment of valley selectivity across all alloy compositions. There is also a clear trend of decrease in the bandgap value with the increasing Se content.

p$_x$ (p$_y$) orbitals. This confirms that the symmetry of the wavefunctions that make up the CB and VB along ΓX and ΓY for all alloy compositions remains the same as that of SnS; the irreducible representations of orbitals that make up the CBM and VBM remain the same across all compositions.

Hence, using our previously discussed selection rules (supplementary material, Text S1, adapted from Ref. 13), CB to VB transitions at the valleys can only occur for light polarized along the x and y directions, respectively; valley selectivity is retained across all SnS$_x$Se$_{1-x}$ alloy compositions, in agreement with the experimental results shown above.

We further quantify such retainment of valley selectivity with the figures of merit, the intervalley ($P_{\text{intervalley},\Gamma Y/\Gamma X}$) and intravalley ($P_{\text{intravalley},\Gamma Y/\Gamma X}$) polarization degrees, as defined in our previous work[13] as

$$P_{intervalley,\Gamma X} = \frac{I_{\Gamma X\|}(\theta = 90°) - I_{\Gamma Y\|}(\theta = 90°)}{I_{\Gamma X\|}(\theta = 90°) + I_{\Gamma Y\|}(\theta = 90°)} \quad \text{and}$$

$$P_{intervalley,\Gamma Y} = \frac{I_{\Gamma Y\|}(\theta = 0°) - I_{\Gamma X\|}(\theta = 0°)}{I_{\Gamma Y\|}(\theta = 0°) + I_{\Gamma X\|}(\theta = 0°)},$$

$$P_{intravalley,\Gamma X} = \frac{I_{\Gamma X\|}(\theta = 90°) - I_{\Gamma X\perp}(\theta = 90°)}{I_{\Gamma X\|}(\theta = 90°) + I_{\Gamma X\perp}(\theta = 90°)} \quad \text{and}$$

$$P_{intravalley,\Gamma Y} = \frac{I_{\Gamma Y\|}(\theta = 0°) - I_{\Gamma Y\perp}(\theta = 0°)}{I_{\Gamma Y\|}(\theta = 0°) + I_{\Gamma Y\perp}(\theta = 0°)}.$$

It is clear from Fig. 3(b) that $P_{\text{intervalley},\Gamma Y/\Gamma X}$ [Fig. 4(a)] remains significant across all compositions. The results from PL measurements conducted under cross polarization were then used to calculate $P_{\text{intravalley},\Gamma Y/\Gamma X}$, which are also presented in Fig. 4(a). The strong polarization degrees of, for example, up to 91% and an average of 75% for $P_{\text{intravalley},\Gamma X}$, proves that the alloys still rival results obtained using monolayer TMDCs from experiments conducted at cryogenic temperatures.[9,12,32]

Our PL, white light R and T, and theoretical results clearly show tunable, wavelength-dependent, non-degenerate valleytronics in SnS$_x$Se$_{1-x}$. For practical purposes, it is thus important to apply Vegard's law[33] to generate a database for the bandgap values and the bowing parameter, b.[34] Figure 4(b) shows the optical bandgap values obtained via white light R and T, as well as PL for both valleys, plotted in compositional space. Using

$$E_{g,SnS_xSe_{1-x}} = xE_{g,SnS} + (1-x)E_{g,SnSe} + bx(1-x),$$

we obtained b$_{,\Gamma Y(\text{white light})}$ = −0.11185 eV, b$_{,\Gamma X(\text{white light})}$ = −0.0331 eV, b$_{,\Gamma Y(\text{PL})}$ = −0.06843 eV, and b$_{,\Gamma X(\text{PL})}$ = −0.0521 eV. The fitted functions are also overlaid in Fig. 4(b). We note that the bowing parameters obtained for the valleys using both absorption and PL methods are close to each other and very small,[35] which gives a rather linear relationship that simplifies the tunability. Calculated bandgap (obtained from Fig. S1) values are also presented in the inset of Fig. 4(b).

However, beyond the scope of this work, we also observe from Figs. 3(b) and S5 that the full-width at half-maximum (FWHM) of the PL peaks [Figs. S6(a) and S6(b)] increases with a greater Se content, along with a decrease in PL intensity [Fig. S6(c)]. We further conducted power-dependent PL measurements, fitted, and analyzed the PL peak intensity using a power law, $I_{PL} \propto I_{excitation}{}^k$, as presented in

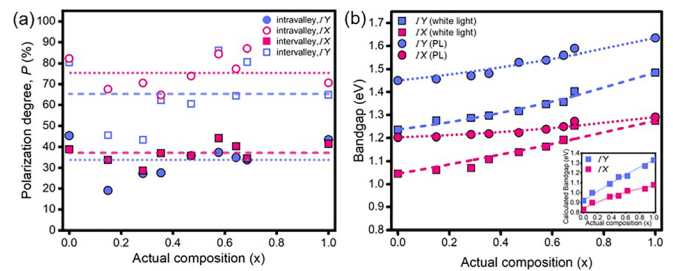**FIG. 4.** Valley selectivity in SnS$_x$Se$_{1-x}$. (a) Trends in polarization degrees with the compositional variation, showing the retainment of high valley selectivity across all alloy compositions in SnS$_x$Se$_{1-x}$. Intervalley (intravalley) polarization degrees are presented as squares (circles), with dashed (dotted) lines demarcating the respective average values. Solid and open data points denote the polarization degrees that depend predominantly on the PL signals of the ΓY and ΓX valleys, respectively. (b) Optical bandgaps obtained by white light R and T and PL measurements, plotted with fitting functions using Vegard's law. Calculated bandgap values are presented in the inset, showing a smooth variation and similar trends for both ΓY and ΓX valleys, respectively.

the supplementary material, Text S2 and Fig. S6(d), to understand the effect on the nature of the bandgap transitions with alloying.

In conclusion, we have conducted reflection/transmission and PL measurements that show the tunability of the two bandgaps from 1.28 eV to 1.05 eV and 1.48 eV to 1.24 eV in bulk SnS_xSe_{1-x} for the valleys residing along ΓX and ΓY, respectively. These valleys retained the selection rules as previously reported in bulk SnS, under ambient conditions and without additional biases. The valleys are strongly and solely excited by y- and x-polarized light and also mostly emit y- and x-polarized light, respectively, effectively serving as a demonstration of tunability of non-degenerate valleys. Our model system also has, nominally, the advantage of superior polarization degrees of up to 91%. We also elucidate the bandgap bowing parameters for the alloy system and revealed some insights into the transitions, including quantitative analyses that revealed recombination mechanisms to be dominantly independent of dopants levels. Such a discovery may allow future work on practical applications with SnS_xSe_{1-x} as a model system to be conducted.

See the supplementary material for the power law analyses of CB to VB transitions, which further explains bandgap transitions and supporting SEM, Raman, and DFT evidence.

AUTHOR'S CONTRIBUTION

J.Y. coordinated the work. S.L. and J.Y. designed the experiments. S.L. conducted the optical measurements and analyzed the data. T.W.H. and E.M.C. conducted the optical measurements. T.H. and K.P. carried out the DFT calculations and electric dipole analysis. Z.F., C.H.S., C.Y., R.L., and Y.L. synthesized and characterized the materials. S.L. and J.Y. wrote the manuscript with the help from all authors. S.L. and Z.F. contributed equally to this work.

REFERENCES

[1] J. R. Schaibley, H. Yu, G. Clark, P. Rivera, J. S. Ross, K. L. Seyler, W. Yao, and X. Xu, Nat. Rev. Mater. 1, 16055 (2016).
[2] X. Xu, W. Yao, D. Xiao, and T. F. Heinz, Nat. Phys. 10, 343 (2014).
[3] L. J. Sham, S. J. Allen, A. Kamgar, and D. C. Tsui, Phys. Rev. Lett. 40, 472 (1978).
[4] K. Takashina, Y. Ono, A. Fujiwara, Y. Takahashi, and Y. Hirayama, Phys. Rev. Lett. 96, 236801 (2006).
[5] Y. P. Shkolnikov, E. P. De Poortere, E. Tutuc, and M. Shayegan, Phys. Rev. Lett. 89(22), 226805 (2002).
[6] O. Gunawan, Y. P. Shkolnikov, K. Vakili, T. Gokmen, E. P. De Poortere, and M. Shayegan, Phys. Rev. Lett. 96, 186404 (2006).
[7] J. Isberg, M. Gabrysch, J. Hammersberg, S. Majdi, K. K. Kovi, and D. J. Twitchen, Nat. Mater. 12, 760 (2013).
[8] A. Rycerz, J. Tworzydło, and C. W. J. Beenakker, Nat. Phys. 3, 172 (2007).
[9] H. Zeng, J. Dai, W. Yao, D. Xiao, and X. Cui, Nat. Nanotechnol. 7, 490 (2012).
[10] D. Xiao, G. Bin Liu, W. Feng, X. Xu, and W. Yao, Phys. Rev. Lett. 108, 196802 (2012).
[11] W. T. Hsu, Y. L. Chen, C. H. Chen, P. S. Liu, T. H. Hou, L. J. Li, and W. H. Chang, Nat. Commun. 6, 8963 (2015).
[12] K. F. Mak, K. He, J. Shan, and T. F. Heinz, Nat. Nanotechnol. 7, 494 (2012).
[13] S. Lin, A. Carvalho, S. Yan, R. Li, S. Kim, A. Rodin, L. Carvalho, E. M. Chan, X. Wang, A. H. Castro Neto, and J. Yao, Nat. Commun. 9, 1455 (2018).
[14] Q. Feng, N. Mao, J. Wu, H. Xu, C. Wang, J. Zhang, and L. Xie, ACS Nano 9, 7450 (2015).
[15] C. S. Jung, F. Shojaei, K. Park, J. Y. Oh, H. S. Im, D. M. Jang, J. Park, and H. S. Kang, ACS Nano 9, 9585 (2015).
[16] S. Susarla, A. Kutana, J. A. Hachtel, V. Kochat, A. Apte, R. Vajtai, J. C. Idrobo, B. I. Yakobson, C. S. Tiwary, and P. M. Ajayan, Adv. Mater. 29, 1702457 (2017).
[17] M. Zhang, J. Wu, Y. Zhu, D. O. Dumcenco, J. Hong, N. Mao, S. Deng, Y. Chen, Y. Yang, C. Jin, S. H. Chaki, Y. S. Huang, J. Zhang, and L. Xie, ACS Nano 8, 7130 (2014).
[18] I. Vurgaftman, J. R. Meyer, and L. R. Ram-Mohan, J. Appl. Phys. 89, 5815 (2001).
[19] L. C. Gomes and A. Carvalho, Phys. Rev. B 92, 085406 (2015).
[20] L. Makinistian and E. A. Albanesi, Phys. Status Solidi B 246, 183 (2009).
[21] D. K. Ferry, Semiconductor: Bonds and Bands (IOP Publishing Ltd., Bristol, 2013).
[22] H. R. Chandrasekhar, R. G. Humphreys, U. Zwick, and M. Cardona, Phys. Rev. B 15, 2177 (1977).
[23] T. H. Patel, R. Vaidya, and S. G. Patel, Bull. Mater. Sci. 26, 569 (2003).
[24] V. Piacente, S. Foglia, and P. Scardala, J. Alloys Compd. 177, 17 (1991).
[25] F. Zocchi and V. Piacente, J. Mater. Sci. Lett. 14, 235 (1995).
[26] J. Xia, X. Z. Li, X. Huang, N. Mao, D. D. Zhu, L. Wang, H. Xu, and X. M. Meng, Nanoscale 8, 2063 (2016).
[27] X. Xu, Q. Song, H. Wang, P. Li, K. Zhang, Y. Wang, K. Yuan, Z. Yang, Y. Ye, and L. Dai, ACS Appl. Mater. Interfaces 9, 12601 (2017).
[28] Q. Li, A. Wei, J. Lu, L. Tao, Y. Yang, D. Luo, J. Liu, Y. Xiao, Y. Zhao, and J. Li, Adv. Electron. Mater. 4, 1800154 (2018).
[29] J. H. Ahn, M. J. Lee, H. Heo, J. H. Sung, K. Kim, H. Hwang, and M. H. Jo, Nano Lett. 15, 3703 (2015).
[30] Z. Mutlu, R. J. Wu, D. Wickramaratne, S. Shahrezaei, C. Liu, S. Temiz, A. Patalano, M. Ozkan, R. K. Lake, K. A. Mkhoyan, and C. S. Ozkan, Small 12, 2998 (2016).
[31] Y. Chen, D. O. Dumcenco, Y. Zhu, X. Zhang, N. Mao, Q. Feng, M. Zhang, J. Zhang, P. H. Tan, Y. S. Huang, and L. Xie, Nanoscale 6, 2833 (2014).
[32] B. Zhu, H. Zeng, J. Dai, Z. Gong, and X. Cui, Proc. Natl. Acad. Sci. 11, 11606 (2014).
[33] L. Vegard, Z. Phys. 17, 5 (1921).
[34] R. E. Nahory, M. A. Pollack, W. D. Johnston, and R. L. Barns, Appl. Phys. Lett. 33, 659 (1978).
[35] S. Adachi, Springer Handbook of Electronic and Photonic Materials (Springer International Publishing, Switzerland, 2017), p. 733.